Journal of Asian Earth Sciences 159 (2018) 60–68

Contents lists available at ScienceDirect

Journal of Asian Earth Sciences

journal homepage: www.elsevier.com/locate/jseaes

Full length article

Transdimensional inversion of scattered body waves for 1D S-wave velocity structure – Application to the Tengchong volcanic area, Southwestern China

Mengkui Li[a,b,*], Shuangxi Zhang[a,b,c,*], Thomas Bodin[d], Xu Lin[e], Tengfei Wu[a]

[a] Department of Geophysics, School of Geodesy and Geomatics, Wuhan University, Wuhan, China
[b] Key Laboratory of Geospace Environment and Geodesy of Ministry of Education, Wuhan University, Wuhan, China
[c] Collaborative Innovation Center of Geospatial Technology, Wuhan, China
[d] Univ Lyon, Université Lyon 1, ENS de Lyon, CNRS, UMR 5276 LGL-TPE, F-69622, Villeurbanne, France
[e] College of Earth Sciences, Chengdu University of Technology, Chengdu, China

ARTICLE INFO

Keywords:
Bayesian inference
Inverse theory
Waveform fitting
Crustal structure

ABSTRACT

Inversion of receiver functions is commonly used to recover the S-wave velocity structure beneath seismic stations. Traditional approaches are based on deconvolved waveforms, where the horizontal component of P-wave seismograms is deconvolved by the vertical component. Deconvolution of noisy seismograms is a numerically unstable process that needs to be stabilized by regularization parameters. This biases noise statistics, making it difficult to estimate uncertainties in observed receiver functions for Bayesian inference. This study proposes a method to directly invert observed radial waveforms and to better account for data noise in a Bayesian formulation. We illustrate its feasibility with two synthetic tests having different types of noises added to seismograms. Then, a real site application is performed to obtain the 1-D S-wave velocity structure beneath a seismic station located in the Tengchong volcanic area, Southwestern China. Surface wave dispersion measurements spanning periods from 8 to 65 s are jointly inverted with P waveforms. The results show a complex S-wave velocity structure, as two low velocity zones are observed in the crust and uppermost mantle, suggesting the existence of magma chambers, or zones of partial melt. The upper magma chambers may be the heart source that cause the thermal activity on the surface.

1. Introduction

Receiver functions (RFs) contain information on seismic structure beneath receivers. They are computed by deconvoluting the vertical components of body wave seismograms from the horizontal component (Vinnik et al., 1977; Langston, 1979; Ammon, 1991; Bostock, 1998). Observed receiver functions can then be inverted to constrain the S-wave velocity (*Vs*) structure beneath the station (Julià et al., 2000; Li and Mashele, 2009; Hammond et al., 2011; Hammond, 2014; Reeves et al., 2015). Various approaches have been implemented, including linearized inversions (Julià et al., 2000; Herrmann and Ammon, 2002; Sosa et al., 2014; Chen et al., 2015, 2016; Li et al., 2016) and non-linear inversions (Sambridge, 1999a; Lawrence and Shearer, 2006; Shen et al., 2016a,b; Kim et al., 2016).

Linearized inversion techniques are based on partial derivatives and the solution model get easily trapped by local minima of the misfit function. Moreover, the final results of linearized inversion strongly depend on the initial model (Julià et al., 2000; Sosa et al., 2014; Wu et al., 2016). Non-linear global optimization techniques, such as genetic algorithm (Shibutani et al., 1996) or simulated annealing (Vinnik et al., 2004), have the ability to efficiently search for a global optimal solution in a highly-dimensional model space. However, these Monte Carlo methods only provide a single best fitting model and fail at representing uncertainty estimates. To overcome this problem, ensemble inference techniques based on a Bayesian formulation of the inverse problem can be used (Mosegaard and Tarantola, 1995; Gallagher et al., 2009; Ball et al., 2014). These ensemble inference techniques provide an ensemble of models sampled from the posterior probability distribution (PPD) using important sampling algorithms, for example the Metropolis-Hasting (M-H) algorithm (Hastings, 1970). The ensemble of models in the solution is used to quantify the credibility of model parameters, providing not only parameters' estimation but also posterior variance and correlation estimates. In recent years, ensemble based Bayesian Monte Carlo techniques have been expanded to the transdimensional case, where the dimension of model space (e.g. number of layers) is unknown and variable (Green, 1995, 2003). After the earliest application of transdimensional Bayesian inversion (TBI) by Malinverno (2002) to solve the inverse problem of DC resistivity sounding, Piana

* Corresponding authors at: Department of Geophysics, School of Geodesy and Geomatics, Wuhan University, Wuhan, China.
E-mail addresses: mkli@sgg.whu.edu.cn (M. Li), shxzhang@sgg.whu.edu.cn (S. Zhang).

https://doi.org/10.1016/j.jseaes.2018.03.015
Received 19 September 2017; Received in revised form 12 March 2018; Accepted 19 March 2018
Available online 22 March 2018
1367-9120/

Agostinetti and Malinverno (2010) firstly applied this technique to the inversion of RF, where the number of layers was simultaneously inverted with *Vs* values. Transdimensional inversion is becoming popular in the geoscience community, attracting increasing interest due to its flexibility for model parameterization (Malinverno, 2002; Sambridge et al., 2006, 2013; Bodin and Sambridge, 2009; Piana Agostinetti and Malinverno, 2010, Dettmer et al., 2010, 2012, 2015; Gallagher et al., 2011; Petrescu et al., 2016; Zheng et al., 2017).

Differing from linearized and traditional non-linear optimization methods, data uncertainty estimates become vital in Bayesian inference (Gouveia and Scales, 1998). Estimated data errors directly control the form of posterior probability distribution. In a transdimensional formulation, data uncertainty plays an even more critical role, as it directly controls the number of parameters in the solution models, that is the complexity of the model space (Piana Agostinetti and Malinverno, 2010; Bodin et al., 2012). Different sources of errors can contribute to data noise, and each of them has different statistical characteristics. The commonly assumed Gaussian white noise, represented by a diagonal covariance matrix, is not accurate enough to describe uncertainties in observed RFs (Sambridge, 1999a; Piana Agostinetti and Malinverno, 2010; Kolb and Lekić, 2014). Instead, the errors contained in RFs are intrinsically correlated in time due to the deconvolution process within limited frequency band (Piana Agostinetti and Malinverno, 2010). Bodin et al. (2012) expanded TBI to the hierarchical case where the variance and correlation of data errors are all treated as unknowns, assuming a Gaussian correlation function. However, the deconvolution process biases noise statistics in RFs, making it difficult to describe the noise in deconvolved waveforms with simple statistics. By looking at the noise statistics of a large number of realizations for noisy RFs, the covariance matrix of data errors cannot be simply parameterized with a Gaussian correlation function. Dettmer et al. (2012) proposed a procedure to estimate the full data covariance matrix by using an arbitrarily high-order autoregressive error model. Although this procedure is promising at first sight, it assumes an exponential decay for the correlation function, which may not be appropriate for receiver functions.

To address these issues, Bodin et al. (2014) proposed an inversion scheme based on a cross-convolution misfit function, where no deconvolution is needed (Menke and Levin, 2003). This technique has recently been used to constrain the upper mantle structure across North America (Calò et al., 2016), and updated to also include SKS waveforms to constrain anisotropic layering (Bodin et al., 2016). However, this cross-convolution misfit function is not a direct data fit (i.e. the difference between observed and modeled data), but rather a conveniently defined cost function, and it cannot be used to construct a proper likelihood function for Bayesian inference (Frederiksen and Delaney, 2015). More recently, Dettmer et al. (2015) proposed a fully Bayesian direct-seismogram inversion technique for receiver-side structure, where the deconvolution was avoided by treating the source-time function as an unknown in the inversion.

In this study, we propose an alternative likelihood function for Bayesian inversion of scattered body waves. Our approach avoids deconvolving noisy seismograms, as we directly invert the observed radial seismograms. The estimated radial waveform is generated by convolving the synthetic RF (computed for a given earth model) with the observed vertical waveform. In this way, this misfit function represents a direct fit to the observed radial waveform, and can be used to define a likelihood function for Bayesian inference. We note that this misfit function has already been used by Kolb and Lekić (2014) to solve the deconvolution problem and in many other non-Bayesian inversion studies (Kosarev et al., 1984; Farra et al., 1991; Farra and Vinnik, 2000). Although this misfit function is not new, in this work we use it for the first time for Bayesian inversion of scattered body waves.

2. Methodology

The proposed approach avoids two common problems in receiver function imaging: (1) the deconvolution of noisy signals, and (2) the estimation of errors in observed RFs. The data vector we are trying to fit is the observed radial component $\mathbf{H}_{obs}(t)$. It can be modeled with the following convolution model:

$$\mathbf{H}_{obs}(t) = \mathbf{h}(t, m) * \mathbf{s}(t) + \mathbf{e}_h(t) \tag{1}$$

where $\mathbf{h}(t, m)$ is the radial impulse response, $\boldsymbol{s}(t)$ is the source-time function and $\mathbf{e}_h(t)$ is random noise with covariance $\mathbf{C_h}$. The radial impulse response can be expressed in terms of the vertical response $\mathbf{h}(t,m) = \mathbf{R}(t,m) * \mathbf{v}(t,m)$, where $\mathbf{R}(t,m)$ is the theoretical receiver function or transfer function. A deconvolution is still needed to compute $\mathbf{R}(t,m)$. However, this is a deconvolution of synthetic seismograms, which is stable as there is no noise involved (Dettmer et al., 2015). We can then write:

$$\mathbf{H}_{obs}(t) = \mathbf{R}(t, m) * \mathbf{v}(t, m) * \mathbf{s}(t) + \mathbf{e}_h(t) \tag{2}$$

This model of the horizontal component still involves the unknown source function $\boldsymbol{s(t)}$. But the term $\mathbf{v}(t,m) * \mathbf{s}(t)$ can be estimated from our observed vertical seismogram:

$$\mathbf{V}_{obs}(t) = \mathbf{v}(t, m) * \mathbf{s}(t) + \mathbf{e}_v(t) \tag{3}$$

where $\mathbf{e}_v(t)$ is a random noise with covariance $\mathbf{C_v}$. We then write:

$$\mathbf{H}_{obs}(t) = \mathbf{R}(t, m) * (\mathbf{V}_{obs}(t) + \mathbf{e_v}(t)) + \mathbf{e_h}(t) \tag{4}$$

$$\mathbf{H}_{obs}(t) = \mathbf{R}(t, m) * \mathbf{V}_{obs}(t) + \mathbf{R}(t, m) * \mathbf{e_v}(t) + \mathbf{e_h}(t) \tag{5}$$

and assuming $\mathbf{e_v}(t)$ and $\mathbf{e_h}(t)$ are normally distributed with zero mean and covariance $\mathbf{C_v}$ and $\mathbf{C_h}$, $\mathbf{H}_{obs}(t)$ can be seen as a vector of random variables with mean $\mathbf{R}(t) * \mathbf{V}_{obs}(t)$ and covariance

$$\mathbf{C_d} = cov(\mathbf{H}_{obs}) = cov(\mathbf{R} * \mathbf{e_v}) + cov(\mathbf{e_h}) = \mathbf{M}\mathbf{C_v}\mathbf{M}^T + \mathbf{C_h} \tag{6}$$

where the matrix $\mathbf{M}$ is defined from the vector $\mathbf{R}$ ($\mathbf{M}[i,j] = \mathbf{R}_{i-j}$). We have now a noise model for the observed horizontal component, which allows us to write a likelihood probability distribution for $\mathbf{H}_{obs}$ in Eq. (5).

In this way, we can generate synthetic radial waveforms by convolving observed vertical component waveforms $\boldsymbol{V_{obs}(t)}$ with theoretical RFs $\boldsymbol{R(t,m)}$. For a given earth model $\mathbf{m}$, the misfit function $\boldsymbol{\Phi(t,m)}$ is defined as the Mahalanobis distance between the observed and synthetic radial waveforms (Kolb and Lekić, 2014):

$$\Phi(t, m) = (\mathbf{H}_{obs}(t) - \mathbf{R}(t, m) * \mathbf{V}_{obs}(t))^T \mathbf{C}_d^{-1} (\mathbf{H}_{obs}(t) - \mathbf{R}(t, m) * \mathbf{V}_{obs}(t)) \tag{7}$$

This misfit function represents a waveform fit, and hence has a clearer physical meaning than the one proposed by Bodin et al. (2014). The likelihood function of observed radial waveform for a given earth model is then constructed as:

$$P(H|m) = \frac{1}{\sqrt{(2\pi)^n |\mathbf{C_d}|}} \exp\left\{-\frac{1}{2}((\mathbf{H}_{obs}(t) - \mathbf{R}(t, \mathbf{m}) * \mathbf{V}_{obs}(t))^T \mathbf{C_d}^{-1} ((\mathbf{H}_{obs}(t) - \mathbf{R}(t, \mathbf{m}) * \mathbf{V}_{obs}(t))\right\} \tag{8}$$

where n is the number of data points in $\mathbf{H}_{obs}(t)$.

Although we could use the exact form for $\mathbf{C_d}$, in this work assume that $\mathbf{C_v} = \mathbf{0}$, and simply use $\mathbf{C_d} = \mathbf{C_h}$, as done in Kolb and Lekić (2014). Since the amplitude of horizontal component is much smaller than the one from the vertical component, the noise on the vertical component may be negligible. That is, assuming $\mathbf{C_v} = \mathbf{C_h}$, we have cov $(\mathbf{R} * \mathbf{e_v}) \ll \text{cov}(\mathbf{e_h})$.

We can then solve our waveform inversion problem using transdimensional hierarchical Bayesian inference, as implemented by Bodin et al. (2012). The number of layers and the parameters for characterizing the covariance matrix are all considered as unknowns. We use the spectral approach of Shibutani et al. (1996) to calculate the theoretical

RF ***R(t,m)***. It is computationally fast and has been widely used in Bayesian Monte Carlo approaches for RF inversion (Sambridge, 1999a, 1999b; Piana Agostinetti and Malinverno, 2010; Bodin et al., 2014).

The observed vertical and radial waveforms in equation (7) are obtained by stacking events in a range of back azimuths and slowness (Kumar et al., 2010; Bodin et al., 2014, Dettmer et al., 2015), written as:

$$\mathbf{V}_{obs}(t) = \sum_{i=1}^{M} \mathbf{V}_i(t)$$
$$\mathbf{H}_{obs}(t) = \sum_{i=1}^{M} \mathbf{H}_i(t) \quad (9)$$

where M is the number of stacked events. Summations in Eq. (9) are conducted to enhance the signal-to-noise ratio (SNR) of stacked waveforms. The seismic events are carefully separated into different groups; each of them covers a small range of backazimuths and ray parameters so that the influences of 3-D seismic structure and moveout effect can be ignored. Our observed radial and vertical waveforms are obtained by stacking events in the group that contains most seismic events. For more details about data processing, we refer readers to Bodin et al. (2016).

3. Synthetic examples

In order to examine the feasibility of the proposed approach, we first invert synthetic waveforms generated from an earth model with known isotropic structure, as is shown in Fig. 1a. The model is made of 6 layers, which presents a low *Vs* layer between 15 and 20 km in the crust and a Moho interface at 30 km (Fig. 1a). Radial and vertical waveforms (Fig. 1b and c) are calculated using a reflectivity method, based on the Thomson-Haskell matrix method (Thomson, 1950; Haskell, 1953), in which the multiple conversions and reflections are considered to calculate the full *P* wave. We use Gaussian pulse with width 2.0 s as the source time function to synthetic waveforms. Two cases are studied here, where waveforms are generated by adding different types of noises, which serve as the "observed measurements" for the subsequent testing inversions.

3.1. Synthetic Test 1

In this test, a Gaussian white (not correlated) noise with standard deviation of 3 percent of the maximum value of the vertical waveform is added to both components. Noise in the inversion is parameterized as an independent and normally distributed random error with standard deviation σ, that is the covariance matrix of data errors $\mathbf{C}_d$ in the inversion is diagonal with diagonal elements equal to σ. The noisy radial waveform (black) and best fitting waveform (red) in Test 1 are shown in Fig. 2a. Since the statistics of the added noise and the parameterized noise in inversion are the same, this test can be seen as a best-case scenario, serving as a proof-of-concept to our approach. The number of layers varied from 2 to 50 in this transdimensional sampling (the true layer number is 6). The values of *Vs* changed in the range of 1.6–6.0 km s^{-1}. The inversion is performed on 120 parallel CPUs to allow large numbers of independent Markov chains, starting at different random points and sampling the model space simultaneously and independently. Each chain is run for 1×10^6 steps in total, in which the first 5×10^5 steps are discarded as burn-in steps. After burn-in period, every 100th model visited is selected for the ensemble to eliminate dependent samples. Some indicators, such as acceptance rates, are used to monitor the convergence of the method, as described by Bodin et al. (2012).

Posterior inference contains an ensemble of 6×10^5 models and the results are shown in Fig. 3. Density plot of the ensemble allows visualizing the distribution of ensemble solution, as shown in Fig. 3a. It represents the posterior probability of *Vs* at each depth and demonstrates the constraints on *Vs*. Fig. 3b shows the posterior mean and maximum *Vs* models together with the true and reference models. The mean model, calculated from the ensemble solution, matches the true model. Fig. 3c denotes the marginal posterior distribution on the interfaces in the model ensemble. For each depth, the value represents the probability for an interface and the width of posterior distribution illustrates the ability to recover it. Flatter and wider posterior distribution means lower probability of an interface existence as well as higher uncertainty to recover it. This case illustrates the ability of the proposed method for posterior uncertainty quantification.

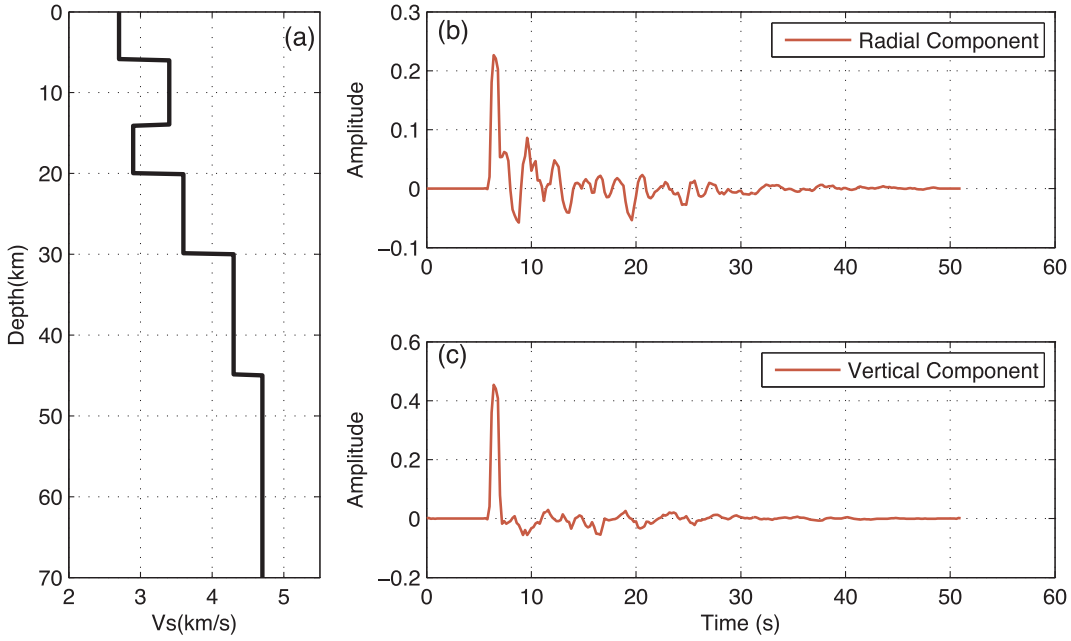

Fig. 1. A synthetic isotropic earth model of 6 layers (a), and synthetic radial waveform (b) and vertical waveform (c). Here, waveforms are noise free and calculated with a ray parameter of 0.08 s km^{-1}. The last layer is an infinite half space.

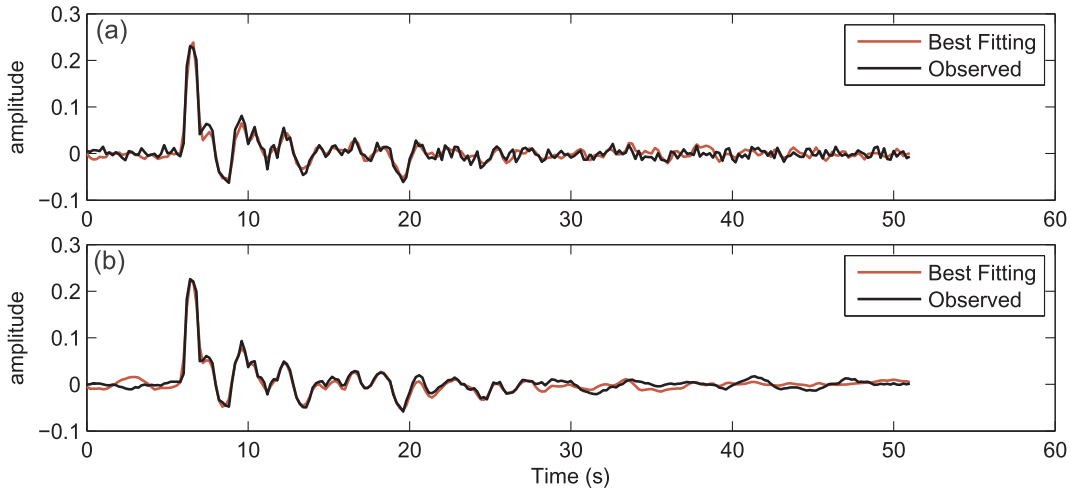

Fig. 2. Noisy and best fitting radial component waveforms for synthetic Test 1 (a) and Test 2 (b).

3.2. Synthetic Test 2

A more realistic correlated noise is now generated to contaminate the synthetic radial waveforms for Test 2. The noisy (black) and best fitting (red) radial waveforms in this test are shown in Fig. 2b. We use a covariance matrix $C_{D_{ij}} = \sigma^2 L_{ij}$, proposed by Kolb and Lekić (2014), to generate the correlated noises. The same as in Test 1, σ here is the standard deviation of added noise and it equals to 3 percent of the maximum value of the vertical waveform. The L_{ij} is a function of absolute lag time $|t_i - t_j|$ and defined as $L_{ij} = e^{-\lambda|t_j - t_i|}\cos(\lambda\omega_0 |t_j - t_i|)$. The values of λ and ω_0 are set to be 0.2 and 4, similarly to Kolb and Lekić (2014) respectively.

For the inversion, we apply the same noise parameterization as in Test 1, i.e. $\mathbf{C}_d$ is set diagonal. In this case, the noise model in the likelihood function does not represent the true noise. As in Test 1, we run the inversion program on 120 parallel CPUs. The number of layers changes between 2 and 50, and all parameters (e.g. number of samples) are kept similar to Test 1.

The inversion results are shown in Fig. 4. The solution is made up of an ensemble of 6×10^5 models. Density plot for *Vs* at each depth is denoted in Fig. 4a; revealing quite good constraint on *Vs* Fig. 4b shows the posterior mean and maximum *Vs* models, together with the true and reference models. The mean model matches the true model, even though we intentionally used an inconsistent noise type from the added noise in the inversion. Fig. 4c denotes the marginal posterior distribution on the interface locations in the ensemble models. The true interfaces are clearly identified and the probability densities at corresponding depths have relatively larger values. It is worth noticing that two extra interfaces (except the interfaces below 60 km) are revealed with low probability densities. This is caused by the underestimation of

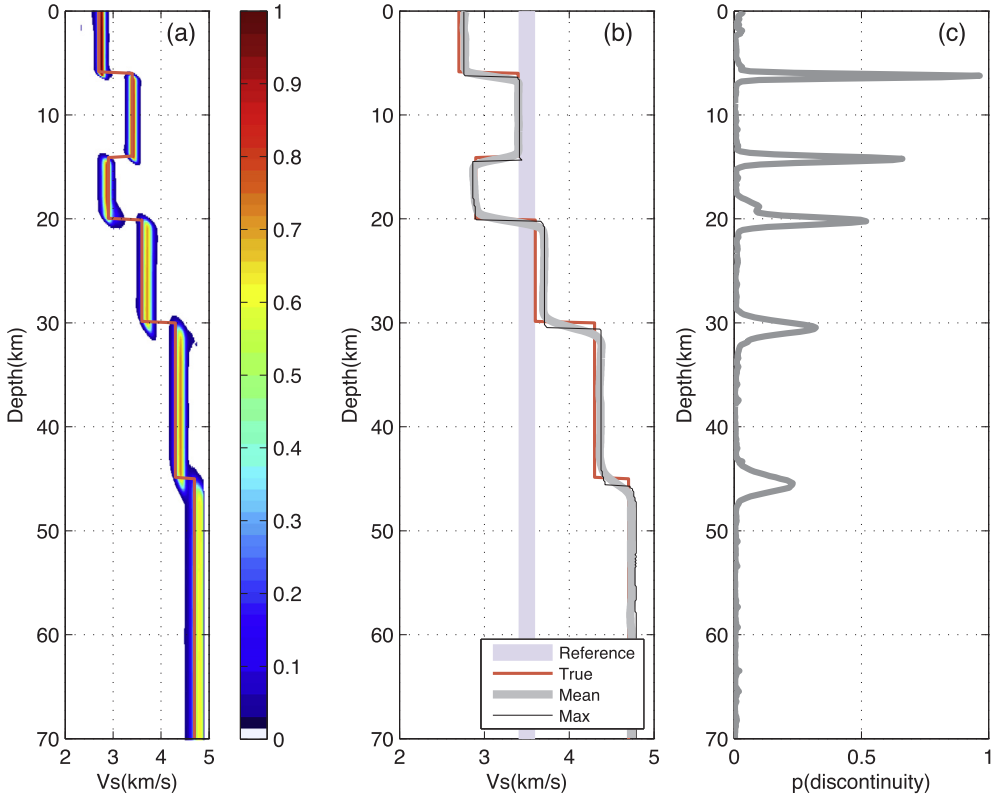

Fig. 3. Inversion results of synthetic Test 1, where the estimated noise used in the inversion is equal to the true synthetic noise. (a) Posterior probability distribution for *Vs* at each depth with true earth model (red line). (b) Gray line: the posterior mean model; Black line: the maximum of marginal posterior model; Red line: the true earth model; Light blue: reference model. (c) Posterior probability for the position of discontinuities. (For interpretation of the references to colour in this figure legend, the reader is referred to the web version of this article.)

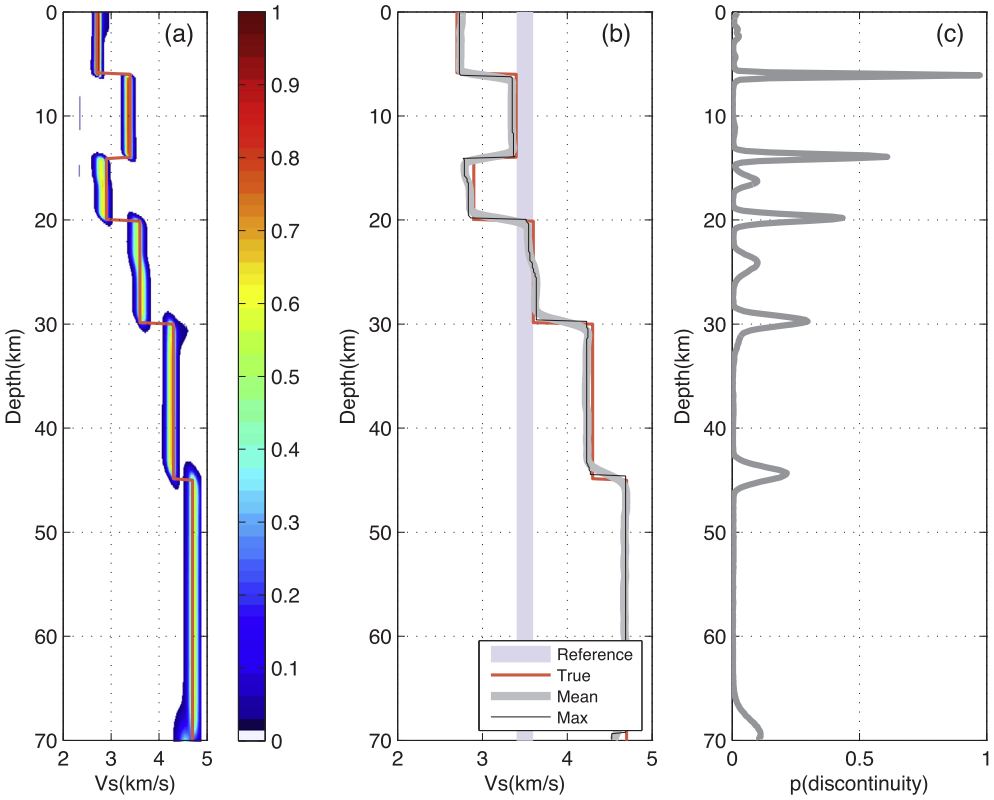

Fig. 4. Inversion results of synthetic Test 2, where the true noise is correlated whereas the noise model in the inversion is assumed uncorrelated. All the results are shown and marked in color lines as the same as that in Fig. 3. (For interpretation of the references to colour in this figure legend, the reader is referred to the web version of this article.)

the true level of noise, resulting in the overestimation of the required data fit, and hence the overestimation of the complexity of model defined by the number of layers (Piana Agostinetti and Malinverno, 2010; Bodin et al., 2012). Our noise-parameterization strategy can only characterize the variance of the true noise, but ignores the correlation property. Despite this defect, the extra interfaces do not bring any obstacles for identifying true interfaces (Fig. 4a and b). A possible improvement could be achieved, albeit at increased computational cost, by parameterizing the noise covariance matrix as $L_{ij} = e^{-\lambda|t_j - t_i|}\cos(\lambda\omega_0|t_j - t_i|)$ where λ and ω_0 are considered as unknown variables to be inverted for. Note that another challenge is to find efficient and fast approaches to calculate the inverse matrix and determinant of data noise covariance matrix, as is shown in Eq. (2).

4. Application to field measurements

4.1. Tectonic background and data

In order to demonstrate the feasibility of our approach on field measurements, we invert for the 1-D *Vs* structure underneath the Tengchong (TC) station. This station is located in the Tengchong Volcanic area, Southwestern China, and belongs to the Tengchong Earthquake-Monitoring Network (Yang et al., 2013). The Tengchong Volcanic area is an important part of the Himalayan geothermal belt. This region is the youngest volcano-active area in Southwestern China (Wang et al., 2003; Wang and Gang, 2004; Yang et al., 2013) and is located on the northeast side of the collision between the Indian and Eurasian plates (Socquet and Pubellier, 2005). Fig. 5a shows the location of the volcanic area. Volcanic eruptions in different epochs cause the possible existence of partial melting zones or magma chambers, characterized by low velocity zones (LVZs) (Wang et al., 2004; Yang et al., 2013; Wu et al., 2016), whose existence is also confirmed by recent geochemical and geophysical studies (Hu et al., 2018; Li et al., 2018). We want to find the locations of hot, partial melting materials generated by past volcanic eruptions.

In this study, we use *P* waveforms of teleseismic events recorded between 2010 and 2014. We select the events having moment magnitude between *Mw* 6.0 and *Mw* 6.1, backazimuths between 90° and 180°, epicentral distances between 30° and 75° to obtain the summed radial and vertical waveforms. The magnitude of selected events should be large enough to ensure good SNR. It also should be close enough to avoid large differences in source character. The distribution of the selected events is shown in Fig. 5b. Waveforms are aligned to the maximum amplitude of *P* arrival peak in order to increase SNR (Kumar et al., 2010). All seismic events are normalized to equal energy and rotated to radial and tangential components. The sign is reversed when the amplitude of the *P* arrival is negative. Events with high noise levels before the first *P* arrival are discarded. A total of 64 events are selected to be stacked for vertical and radial waveforms based on Eq. (9). We stack raw waveforms without band-pass filtering to avoid creating a correlated noise. We show the single (gray) and stacked (red) waveforms used for the transdimensional inversion in Fig. 6.

P to *S* converted phases are sensitive to interfaces at different depths, but poorly constrain absolute velocities. Surface-wave dispersion (SWD) measurements, on the contrary, are sensitive to the absolute *Vs* value, with no sensitivity to discontinuities. Their combination can provide tighter constraints on *Vs* than either method individually (Julià et al., 2000; Sosa et al., 2014; Fontaine et al., 2015; Chen and Niu, 2016; Chong et al., 2016). In this study, we jointly invert the summed radial waveform and fundamental-mode SWD spanning periods from 8 to 65 s (Xie et al., 2013) for *Vs* structure underneath TC.

4.2. Inversion results

We jointly inverted the summed radial waveforms and SWD for *Vs* structure using the proposed method in this study. The V_P/V_S ratio for the entire profile is fixed to the value from *H-k* stacking (Li et al., 2016). The inversion is performed on 160 parallel CPUs, starting at different random points. Each chain is run for 1.2×10^6 steps and the first 6×10^5 steps are discarded as burn-in steps. Posterior inference of this

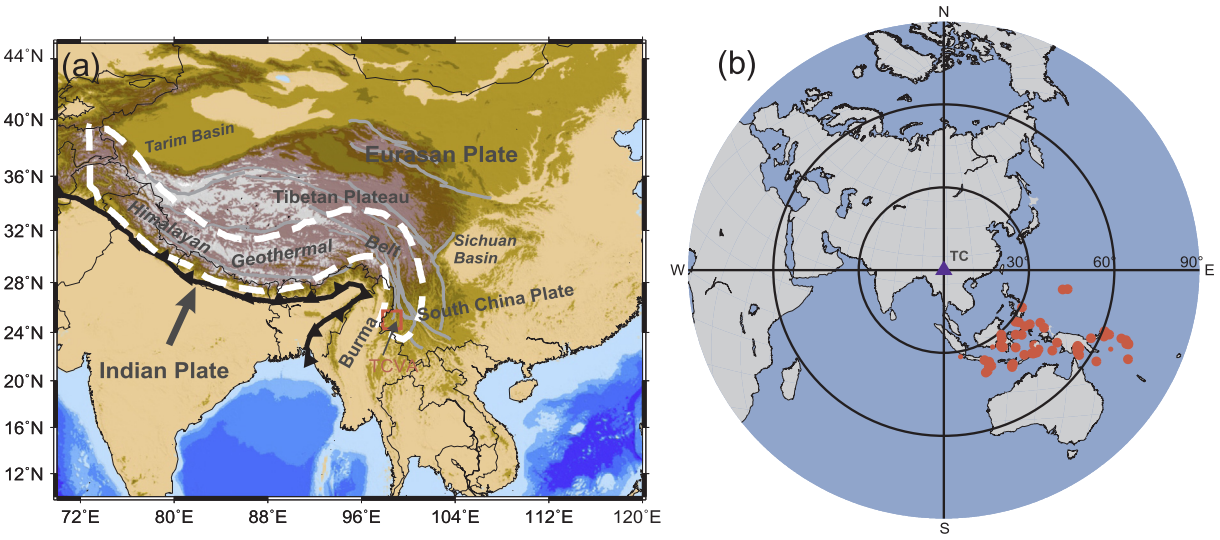

Fig. 5. Locations the Tengchong Volcanic area (a) and the distribution of 64 teleseismic events used in this study with an epicentral distance between 30° and 90° to TC station (b). Blue triangle denotes the station location and red dots represent the selected events. (For interpretation of the references to colour in this figure legend, the reader is referred to the web version of this article.)

inversion consists of an ensemble of 9.6×10^5 models.

The posterior solution is shown in Fig. 7. Fig. 7a shows the density plot of the ensemble of models in the solution, while Fig. 7b shows the posterior mean and maximum *Vs* models. The mean *Vs* model shows a quite complex velocity structure. Almost all the models present a low velocity layer in the first two kilometers, denoting the presence of an unconsolidated sedimentary layer. Both synthetic SWD and radial waveforms match observed data within errors (Fig. 7c and d). In a recent published research conducted by Li et al. (2016) to study the crustal and uppermost mantle S-wave velocity beneath southeastern Tibetan, they jointly inverted the average receiver function and SWD data at station TC for a 1-D velocity profile. We show the velocity profile in Fig. 8 for comparison. Our inversion result is generally consistent with that from the traditional linearized joint inversion (Fig. 8), i.e. the existence of LVZs in crust and uppermost mantle. However, it still shows significant differences, especially the depth range of LVZs. As stated in Li et al. (2016), the receiver function at each station used in their research is the average one from all the receiver functions at different azimuths. The 1-D profiles show only the average structure beneath each station, without considering the possible horizontal variations. However, we used earthquake event data from azimuth between 90° and 180° in this study. The differences may reveal the possible horizontal variations of the S-wave velocity structure beneath this station.

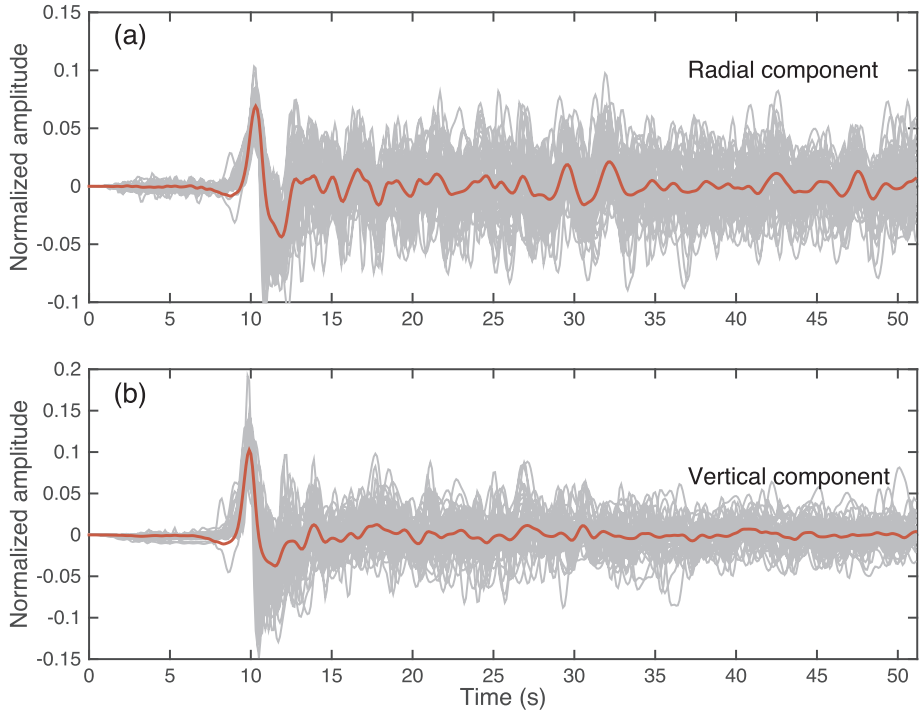

Fig. 6. Single (gray) and stacked (red) waveforms used for the MCMC inversion: (a) radial component; (b) vertical component. (For interpretation of the references to colour in this figure legend, the reader is referred to the web version of this article.)

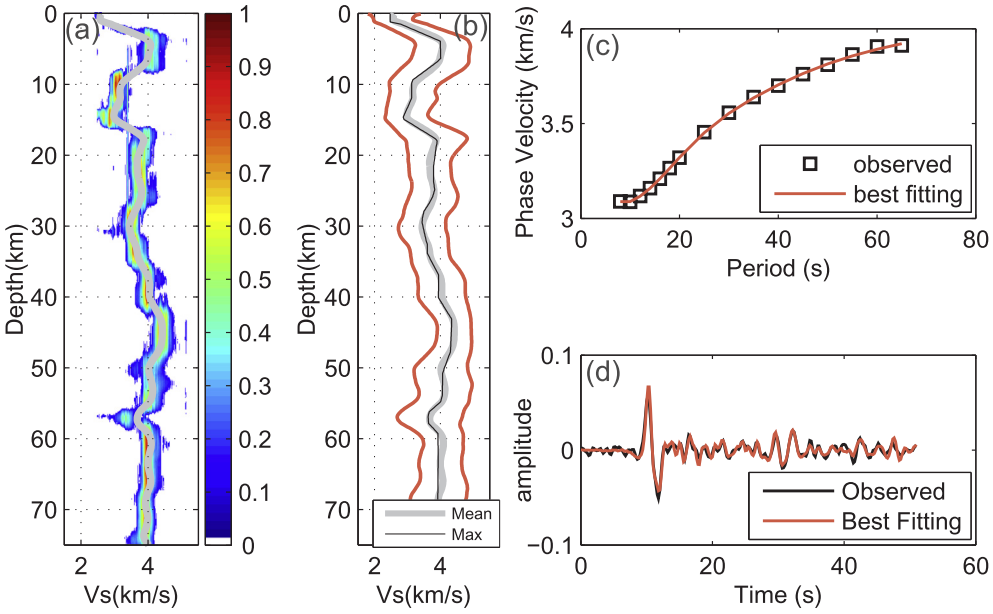

Fig. 7. Joint inversion of summed radial waveform and surface wave dispersion. (a) Posterior probability distribution for *Vs* at each depth with mean earth model (gray line) overlain. (b) Gray line: the posterior mean model; Black line: the maximum of marginal posterior model; Red lines: 95 per cent credible interval. (c) Best fitting (red line) and observed SWD (black squares). (d) Best fitting (red line) and observed waveforms (black line). (For interpretation of the references to colour in this figure legend, the reader is referred to the web version of this article.)

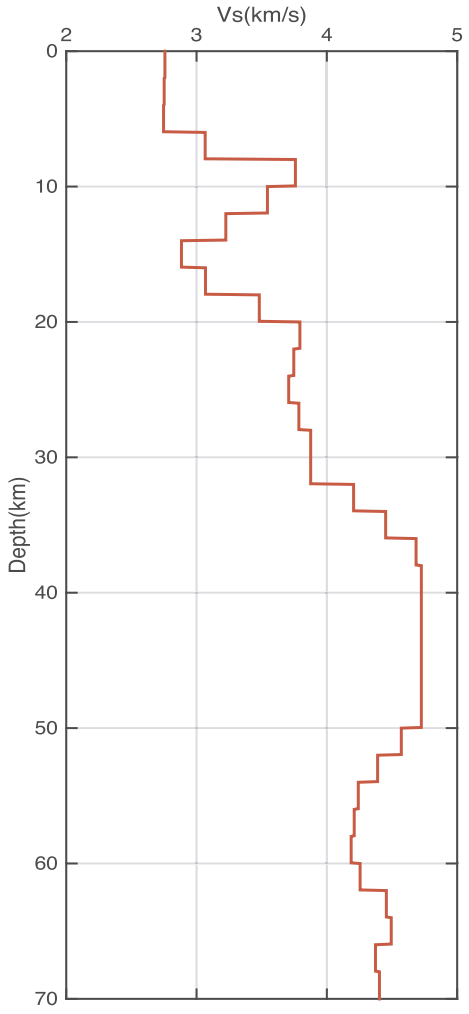

Fig. 8. Inversion result from traditional joint inversion.

5. Discussion

We reveal the 1-D *Vs* structure beneath TC station (Fig. 7a and b) using the fully non-linear Bayesian inversion method proposed in this study. In Fig. 9, we present a cartoon to summarize the findings beneath this station (Fig. 9a) and a simple schematic model to reveal the magma dynamic (Fig. 9b). The results from joint inversion depict the Moho interface down to about 42 km, which is about 6 km deeper than that from *H-k* stacking (Li et al., 2016). Moho depth from *H-k* stacking is an azimuthally averaged estimation, while inversion result denotes the estimation from back azimuths between 90° and 180°. The difference between the two estimations denotes a complex Moho interface, or the presence of strong anisotropy beneath this station. The Moho depth may vary as a function of back azimuth. We find a relative high velocity zone (HVZ) at depth 5–8 km, which is consistent with the results of Cao et al. (2013) from *P* wave tomography. The HVZ could be caused by the cooling of magmas from volcanic eruptions. Two LVZs (marked as LVZ1 and LVZ2 in Fig. 9a) are presented in crust and upper mantle. LVZ1 is located at the depths from ~8 km to ~18 km. It has the largest velocity contrast with surrounding areas, presenting high temperature and strong melting. Similar LVZs in this depth range are also revealed in the previous studies from regional *P* wave tomography (Wang and Gang, 2004) and deep seismic sounding (DSS) (Wang et al., 2003). This LVZ is interpreted as a magma chamber in upper to middle crust (Fig. 9) (Wang et al., 2003; Wang and Gang, 2004; Yang et al., 2013). Previous studies show high thermal activities in this area (i.e. Zhao et al., 2006); this magma chamber may serve well as the heat source. Heat in magma chambers is transferred to earth surface through the heart transfer pipes (Fig. 9b), i.e. cracks in upper crust. Similar to previous studies (Wang et al., 2003; Wang and Gang, 2004; Yang et al., 2013), we find a LVZ in the uppermost mantle depth (Fig. 9; LVZ2), which denotes the existence of partial melting zones in uppermost mantle and caused by the residual magma from volcanic eruptions. Note that the LVZ2 is not so obvious as LVZ1, showing small velocity contrast with surrounding areas. However, the result from traditional joint inversion shows a relatively obvious LVZ in the same depth range (50–60 km). In the depths range from ~25 km to ~36 km, the velocity shows also slight contrast with surrounding areas, which may be far from being defined as an LVZ. It is perhaps influenced by the crustal flow channels in southeastern Tibetan (Zhao et al., 2013; Li et al., 2016). Li et al. (2016) found two crustal low-velocity zones beneath southeastern Tibetan, which were interpreted as two possible migration channels of soft materials. One of the

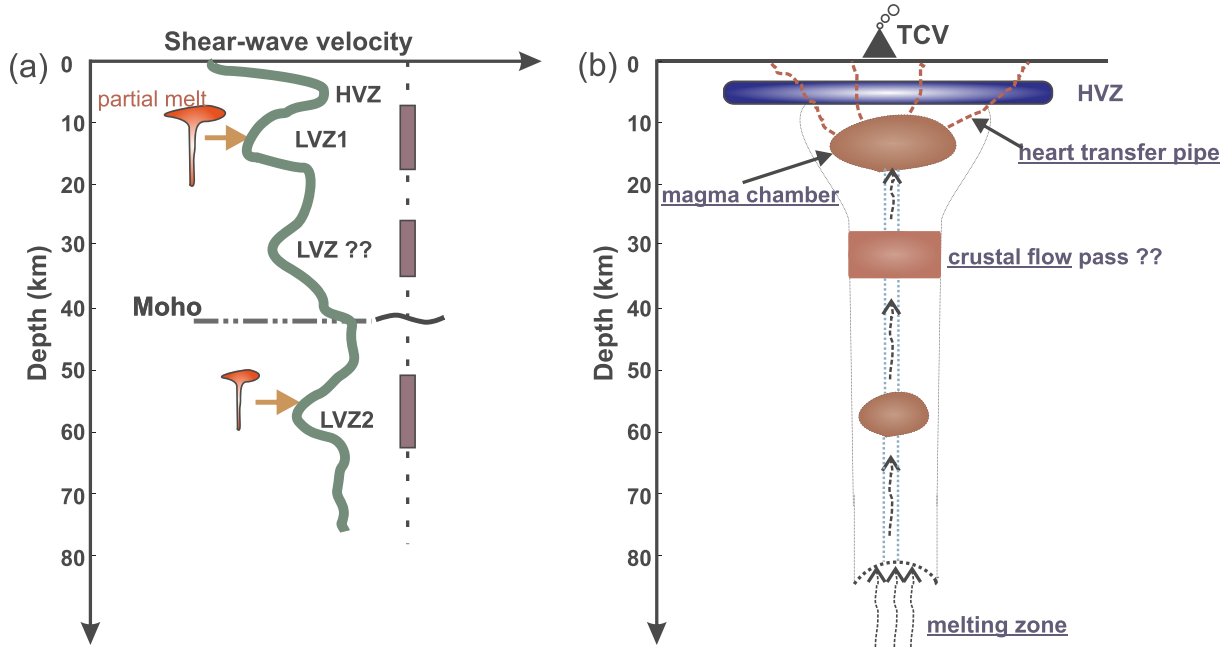

Fig. 9. Cartoon summarizing the findings beneath TC station based on our approach. (a) 1-D shear-wave velocity profile with LVZs distribution; (b) a simple schematic model shows the dynamic model of Tengchong Volcano (TCV). Green conduit represents the passage for magma upwelling and erupting.

channels (channel C1; see Fig. 10 in Li et al., 2016) exactly passes the station.

The inferred *Vs* structure suggests that magma chambers exist in both crust and upper mantle under this station. Fig. 9b presents a simple schematic for dynamic model of Tengchong Volcano. Previous *P* wave tomography results revealed a vertically extending low velocity zone, providing a conduit for magma upwelling and erupting (Lei et al., 2009; Cao et al., 2013). Melting zones in deep mantle provide the original source of magmas (Fig. 9b).

It is worth noticing that we invert *Vs* by fixing V_P/V_S to the predetermined value from *H-k* stacking (Li et al., 2016). Anisotropic layers, as well as dipping interfaces, are neglected even though they have been widely recognized in the crust (Sherrington et al., 2004; Bianchi et al., 2008). These features may produce peculiar *P*-to-*S* conversions which display well-defined back-azimuthal patterns. Future work for improving our method can be done by treating *Vp/Vs* ratio, anisotropic parameters and dipping layers as unknown parameters in the inversion, and jointly inverting several stacked radial and tangential waveforms measured in different ranges of back-azimuths.

6. Conclusion

This study proposes a fully non-linear Bayesian inversion of teleseismic *P* radial waveforms to constrain *Vs* structures. We directly measure the difference between observed and synthetic radial waveforms, and thus avoid the numerically unstable computation of receiver functions. This formulation of the inverse problem allows us to directly account for noise in stacked seismograms without having to model the noise in observed RFs.

Joint inversion of radial *P* seismograms and SWD using our approach reveals the 1-D *Vs* structure beneath TCT station. An unconsolidated sedimentary layer, with thickness about two kilometers, is presented by almost all the final ensemble models. The final results reveal a HVZ at depth 5–8 km, which may be caused by the cooling of magmas from volcano eruptions. There are three LVZs are observed in crustal and upper mantle depths. LVZ1 distributes from ~8 km to ~18 km depth, is a magma chamber caused by volcanic eruptions (Wang et al., 2003; Wang and Gang, 2004; Yang et al., 2013). An interesting LVZ, the LVZ2, is found in upper mantle, denoting the existence of residual magma (magma chamber) in mantle. The inversion results confirm the existence of partial melting zones beneath this station. Moreover, they distribute in both crust and mantle, at least in the uppermost mantle. However, the spatial distribution of partial melt zones (or magma chamber) still needs to be studied with densely distributed seismic stations.

Acknowledgements

We appreciate the Earthquake Administration of Yunnan Province for providing waveform data of TCT station. This study is supported by the 973 Project of China (No. 2013CB733303), the National Natural Science Foundation of China (No. 41704046, 41474093), the China Postdoctoral Science Foundation (No. 201620162016) and the Open Research Fund Program of the Key Laboratory of Geospace Environment and Ministry of Education (No. 16-02-05, 15-01-06). The numerical calculation in this paper have been done on the supercomputing system in the Supercomputing Center of Wuhan University.

References

Ammon, C.J., 1991. The isolation of receiver effects from teleseismic P waveform. Bull. Seism. Soc. Am. 81, 2504–2510.
Ball, J.S., Sheehan, A.F., Stachnik, J.C., Lin, F.C., Collins, J.A., 2014. A joint Monte Carlo analysis of seafloor compliance, Rayleigh wave dispersion and receiver functions at ocean bottom seismic stations offshore New Zealand. Geochem. Geophys. Geosyst. 15, 5051–5068.
Bianchi, I., Piana Agostinetti, N., Chiarabba, C., De Gori, P., 2008. Deep structure of the Colli Albani volcanic district (central Italy) from receiver functions analysis. J. Geophys. Res. 113, B09313.
Bodin, T., Yuan, H.Y., Romanowicz, B., 2014. Inversion of receiver functions without deconvolution – application to the Indian craton. Geophys. J. Int. 196, 1025–1033.
Bodin, T., Sambridge, M., Tkalčić, H., Arroucau, P., Gallagher, K., Rawlinson, N., 2012. Transdimensional inversion of receiver functions and surface wave dispersion. J. Geophys. Res. 117, B02301.
Bodin, T., Sambridge, M., 2009. Seismic tomography with the reversible jump algorithm. Geophys. J. Int. 178, 1411–1436.
Bodin, T., Leiva, J., Romanowicz, B., Maupin, V., Yuan, H., 2016. Imaging anisotropic layering with Bayesian inversion of multiple data types. Geophy. J. Int. 206, 605–629.
Bostock, M., 1998. Mantle stratigraphy and evolution of the Slave province. J. Geophys. Res. 103, 21183–21200.
Calò, M., Bodin, T., Romanowicz, B., 2016. Layered structure in the upper mantle across North America from joint inversion of long and short period seismic data. Earth

Planet. Sci. Lett. 449, 164–175.
Cao, L.M., Xu, Y., Wu, S.G., 2013. Finite difference tomography of the crustal velocity structure in Tengchong, Yunnan Province. Chinese J. Geophys. 56, 1159–1167.
Chen, Y.L., Niu, F.L., 2016. Joint inversion of receiver functions and surface waves with enhanced preconditioning on densely distributed CNDSN stations: crustal and upper mantle structure beneath China. J. Geophys. Res. Solid Earth 121, 743–766.
Chen, H., Zhu, L., Ye, Q., Wang, Q., Yang, Y., Zhang, P., 2015. Azimuthal anisotropy of the crust and uppermost mantle in northeast North China Craton from inversion of Rayleigh wave phase velocity. Geophy. J. Int. 202, 624–639.
Chen, H., Zhu, L., Su, Y., 2016. Low velocity crustal flow and crust–mantle coupling mechanism in Yunnan, SE Tibet, revealed by 3D S-wave velocity and azimuthal anisotropy. Tectonophysics 685, 8–20.
Chong, J., Ni, S., Chu, R., Somerville, P., 2016. Joint inversion of body-wave receiver function and rayleigh-wave ellipticity. Bull. Seism. Soc. Am. 106, 537–551.
Dettmer, J., Molnar, S., Steininger, G., Dosso, S.E., Cassidy, J.F., 2012. Trans-dimensional inversion of microtremor array dispersion data with hierarchical autoregressive error models. Geophys. J. Int. 188, 719–734.
Dettmer, J., Dosso, S., Holland, C., 2010. Trans-dimensional geoacoustic inversion. J. Acoust. Soc. Am. 128, 3393–3405.
Dettmer, J., Dosso, S., Bodin, T., Stipevic, J., Cummins, P.R., 2015. Direct-seismogram inversion for reveiver-side structure with uncertain source-time functions. Geophys. J. Int. 203, 1373–1387.
Farra, V., Vinnik, L., 2000. Upper mantle stratication by P and S receiver functions. Geophys. J. Int. 141, 699–712.
Farra, V., Vinnik, L., Romanowicz, B., Kosarev, G., Kind, R., 1991. Inversion of teleseismic S particle motion for azimuthal anisotropy in the upper mantle: a feasibility study. Geophys. J. Int. 106, 421–431.
Frederiksen, A.W., Delaney, C., 2015. Deriving crustal properties from the P Coda without deconvolution: the southwestern Superior Province, North America. Geophys. J. Int. 201, 1491–1506.
Fontaine, F.R., Barruol, G., Tkalčić, H., Wölbern, I., Rümpker, G., Bodin, T., Haugmard, M., 2015. Crustal and uppermost mantle structure variation beneath La Réunion hotspot track. Geophys. J. Int. 203, 107–126.
Gallagher, K., Charvin, K., Nielsen, S., Sambridge, M., Stephenson, J., 2009. Markov chain Monte Carlo (McMC) sampling methods to determine optimal models, model resolution and model choice for earth science problems. J. Mar. Petrol. Geol. 26, 525–535.
Gallagher, K., Bodin, T., Sambridge, M., Weiss, D., Kylander, M., Large, D., 2011. Inference of abrupt changes in noisy geochemical records using Bayesian Transdimensional changepoint models. Earth Planet. Sci. Lett. 311, 182–194.
Gouveia, W., Scales, J., 1998. Bayesian seismic waveform inversion Parameter estimation and uncertainty analysis. J. Geophys. Res. 103, 2759–2780.
Green, P., 2003. Trans-dimensional Markov chain Monte Carlo. Highly Struct. Stochastic Syst. 27, 179–198.
Green, P.J., 1995. Reversible jump Markov chain Monte Carlo computation and Bayesian model determination. Biometrika 82, 711–732.
Hammond, J.O.S., Kendall, J.M., Stuart, G.W., Keir, D., Ebinger, C., Ayele, A., Belachew, M., 2011. The nature of the crust beneath the Afar triple junction: evidence from receiver functions. Geochem. Geophys. Geosyst. 12, Q12004.
Hammond, J.O.S., 2014. Constraining melt geometries beneath the Afar Depression, Ethiopia from teleseismic receiver functions: the anisotropic H-k stacking technique. Geochem. Geophys. Geosyst. 15, 1316–1332.
Haskell, N., 1953. The dispersion of surface waves on multilayered media. Bull. Seis. Soc. Am. 43, 17–34.
Hastings, W.K., 1970. Monte Carlo sampling methods using Markov chains and their applications. Biometrika 57, 97–109.
Herrmann, R.B., Ammon, C.J., 2002. Computer Programs in Seismology: Surface Wave, Receiver Function and Crustal Structure. Saint Louis University, St. Louis, MO, USA.
Hu, J.H., Song, X.Y., He, H.L., Zheng, W.Q., Yu, S.Y., Chen, L.M., Lai, C.K., 2018. Constraints of texture and composition of clinopyroxene phenocrysts of Holocene volcanic rocks on a magmatic plumbing system beneath Tengchong, SW China. J. Asian Earth Sci. 154, 342–353.
Julià, J., Ammon, C.J., Herrmann, R.B., Correig, A.M., 2000. Joint inversion of receiver functions and surface wave dispersion observations. Geophys. J. Int. 143, 99–112.
Kim, S., Dettmer, J., Rhie, J., Tkalčić, H., 2016. Highly efficient Bayesian joint inversion for receiver-based data and its application to lithospheric structure beneath the southern Korean Peninsula. Geophys. J. Int. 206, 328–344.
Kolb, J.M., Lekić, V., 2014. Receiver function deconvolution using transdimensional hierarchical Bayesian inference. Geophys. J. Int. 197, 1719–1735.
Kosarev, G., Makeyeva, L., Vinnik, L., 1984. Anisotropy of the mantle inferred from observations of P to S converted waves. Geophys. J. Int. 76, 209–220.
Kumar, P., Kind, R., Yuan, X., 2010. Receiver function summation without deconvolution. Geophys. J. Int. 180, 1223–1230.
Langston, C.A., 1979. Structure under mount Rainer, Washington, inferred from teleseismic body waves. J. Geophys. Res. 84, 4749–4762.
Lawrence, J.F., Shearer, P.M., 2006. A global study of transition zone thickness using receiver functions. J. Geophys. Res. 111, B06307.
Lei, J., Zhao, D., Su, Y., 2009. Insight into the origin of the Tengchong intraplate volcano and seismotectonics in southwest China from local and teleseismic data. J. Geophys. Res. 114, B05302.
Li, A., Mashele, B., 2009. Crustal structure in the Pakistan Himalaya from teleseismic receiver functions. Geochem. Geophys. Geosyst. 10, Q12010.
Li, M.K., Zhang, S.X., Wang, F., Wu, T.F., Qin, W.B., 2016. Crustal and upper-mantle structure of the southeastern Tibetan Plateau from joint analysis of surface wave dispersion and receiver functions. J. Asian Earth Sci. 117, 52–63.
Li, M.K., Zhang, S.X., Wu, T.F., Hua, Y.J., Zhang, B., 2018. Fine crustal and uppermost mantle S-wave velocity structure beneath the Tengchong volcanic area inferred from receiver function and surface-wave dispersion: constraints on magma chamber distribution. B. Volcanol. 80, 25.
Malinverno, A., 2002. Parsimonious Bayesian Markov chain Monte Carlo inversion in a nonlinear geophysical problem. Geophys. J. Int. 151, 675–688.
Menke, W., Levin, V., 2003. The cross-convolution method for interpreting SKS splitting observations, with application to one and two-layer anisotropic earth models. Geophys. J. Int. 154, 379–392.
Mosegaard, K., Tarantola, A., 1995. Monte Carlo sampling of solutions to inverse problems. J. Geophys. Res. 100, 12431–12447.
Petrescu, L., Bastow, I.D., Darbyshire, F.A., Gilligan, A., Bodin, T., Menke, W., Levin, V., 2016. Three billion years of crustal evolution in eastern Canada: constraints from receiver functions. J. Geophys. Res. Solid Earth 121, 788–811.
Piana Agostinetti, N., Malinverno, A., 2010. Receiver function inversion by trans-dimensional Monte Carlo sampling. Geophys. J. Int. 181, 858–872.
Reeves, Z., Lekić, V., Schmerr, N., Kohle, M., Weeraratne, D., 2015. Lithospheric structure across the California Continental Borderland from receiver functions. Geochem. Geophys. Geosyst. 16, 246–266.
Sambridge, M., 1999a. Geophysical inversion with a neighborhood algorithm – I. Searching a parameter space. Geophys. J. Int. 138, 479–494.
Sambridge, M., 1999b. Geophysical inversion with a neighborhood algorithm – II. Searching a parameter space. Geophys. J. Int. 138, 727–746.
Sambridge, M., Gallagher, K., Jackson, A., Rickwood, P., 2006. Transdimensional inverse problems, model comparison and the evidence. Geophys. J. Int. 167, 528–542.
Sambridge, M., Bodin, T., Gallagher, K., Tkalčić, H., 2013. Transdimensional inference in the geosciences. Philos. Trans. R. Soc. A 371, 20110547.
Shen, W., Ritzwoller, M.H., 2016a. Crustal and uppermost mantle structure beneath the United States. J. Geophys. Res. Solid Earth 121, 4306–4342.
Shen, W., Ritzwoller, M.H., Kang, D., Kim, Y., Ning, J., Lin, F.-C., Wang, W., Zheng, Y., Zhou, L., 2016b. A seismic reference model for the crust and uppermost mantle beneath China from surface wave dispersion. Geophys. J. Int. 206, 954–979.
Sherrington, H.F., Zandt, G., Frederiksen, A., 2004. Crustal fabric in the Tibetan Plateau based on waveform inversion for seismic anisotropy parameters. J. Geophys. Res. 109, B02312.
Shibutani, T., Sambridge, M., Kennett, B., 1996. Genetic algorithm inversion for receiver functions with application to crust and uppermost mantle structure beneath eastern Australia. Geophys. Res. Lett. 23, 1829–1832.
Socquet, A., Pubellier, M., 2005. Cenozoic deformation in western Yunnan (China - Myanmar) border. J. Asian Earth Sci. 24, 495–515.
Sosa, A., Thompson, L., Velasco, A.A., Romero, R., Herrmann, R.B., 2014. 3-D structure of the Rio Grande Rift from 1-D constrained joint inversion of receiver functions and surface wave dispersion. Earth Planet. Sci. Lett. 402, 127–137.
Thomson, W., 1950. Transmission of elastic waves through a stratified solid medium. J. Appl. Phys. 21, 89–93.
Vinnik, L., Reigber, C., Aleshin, I., Kosarev, G., Kaban, M., Oreshin, S., Roecker, S., 2004. Receiver function tomography of the central Tien Shan. Earth Planet. Sci. Lett. 225, 131–146.
Vinnik, L.P., Lukk, A.A., Nersesov, I.L., 1977. Nature of the intermediate seismic zone in the mantle of Pamirs-Hindu-Kush. Tectonophysics 38, T9–T14.
Wang, C.Y., Gang, H.F., 2004. Crustal structure in Tengchong Volcano-Geothermal Areas, western Yunnan, China. Tectonophysics 380, 69–87.
Wang, C.Y., Chan, W.W., Money, W.D., 2003. Three-dimensional velocity structure of crust and upper mantle in southwestern China and its tectonic implications. J. Geophys. Res. 108, 2442.
Wu, T.F., Zhang, S.X., Li, M.K., Qin, W.B., Zhang, C.Y., 2016. Two crustal flowing channels and volcanic magma migration underneath the SE margin of the Tibetan Plateau as revealed by surface wave tomography. J. Asian Earth Sci. 132, 25–39.
Xie, J., Ritzwoller, M.H., Shen, W., Yang, Y.J., Zheng, Y., Zhou, L., 2013. Crustal radial anisotropy across Eastern Tibet and the Western Yangtze Craton. J. Geophys. Res. Solid Earth 118, 4226–4252.
Yang, H.Y., Hu, J.F., Hu, Y.L., Duan, Y.Z., Li, G.Q., 2013. Crustal structure in the Tengchong volcanic area and position of the magma chambers. J. Asian Earth Sci. 73, 48–56.
Zhao, C., Ran, H., Chen, K., 2006. Present-day magma chambers in Tengchong volcanic area inferred from relative geothermal gradient. Acta Geol. Sin. 22, 1517–1528.
Zhao, L.F., Xie, X.B., He, J.K., Tian, X.B., Yao, Z.X., 2013. Crustal flow pattern beneath the Tibetan Plateau constrained by regional Lg-wave Q tomography. Earth Planet. Sci. Lett. 383, 113–122.
Zheng, D.C., Saygin, E., Cummins, P., Ge, Z.X., Min, Z.X., Cipta, A., Yang, R.H., 2017. Transdimensional Bayesian seismic ambient noise tomography across SE Tibet. J. Asian Earth Sci. 134, 86–93.